Lasers Med Sci (2014) 29:173–183
DOI 10.1007/s10103-013-1306-5

ORIGINAL ARTICLE

Temperature imaging of laser-induced thermotherapy (LITT) by MRI: evaluation of different sequences in phantom

Babak Bazrafshan · Frank Hübner · Parviz Farshid · Renate Hammerstingl · Jijo Paul · Vitali Vogel · Werner Mäntele · Thomas J. Vogl

Received: 24 August 2012 / Accepted: 11 March 2013 / Published online: 28 March 2013

Abstract The purpose of this study was to evaluate magnetic resonance (MR) temperature imaging of the laser-induced thermotherapy (LITT) comparing the proton resonance frequency (PRF) and T_1 thermometry methods. LITT was applied to a liver-mimicking acrylamide gel phantom. Temperature rise up to 70 °C was measured using a MR-compatible fiber-optic thermometer. MR imaging was performed by a 1.5-T scanner utilizing fast gradient echo sequences including a segmented echo planar imaging (seg-EPI) sequence for PRF and the following sequences for T_1 method: fast low-angle shot (FLASH), inversion recovery turbo flash (IRTF), saturation recovery turbo flash (SRTF), and true fast imaging (TRUFI). Temperature-induced change of the pixel values in circular regions of interest, selected on images under the temperature probe tip, was recorded. For each sequence, a calibration constant could be determined to be −0.0088 ± 0.0002 ppm $°C^{-1}$ (EPI), −1.15 ± 0.03 $°C^{-1}$ (FLASH), −1.49 ± 0.03 $°C^{-1}$ (IRTF), −1.21 ± 0.03 $°C^{-1}$ (SRTF), and −2.52 ± 0.12 $°C^{-1}$ (TRUFI). These constants were evaluated in further LITT experiments in phantom comparing the calculated temperatures with the fiber optic-measured ones; temperature precisions of 0.60 °C (EPI), 0.81 °C (FLASH), 1.85 °C (IRTF), 1.95 °C (SRTF), and 3.36 °C (TRUFI) were obtained. Furthermore, performing the Bland–Altman analysis, temperature accuracy was determined to be 0.23 °C (EPI), 0.31 °C (FLASH), 1.66 °C (IRTF), 1.19 °C (SRTF), and 3.20 °C (TRUFI). In conclusion, the seg-EPI sequence was found to be more convenient for MR temperature imaging of LITT due to its relatively high precision and accuracy. Among the T_1 method sequences, FLASH showed the highest accuracy and robustness.

Keywords LITT · MR thermometry · PRF · Thermal ablation · Gel phantom

B. Bazrafshan (✉) · F. Hübner · P. Farshid · R. Hammerstingl · J. Paul · T. J. Vogl
Institute for Diagnostic and Interventional Radiology,
J.W. Goethe-University Hospital,
Theodor-Stern-Kai 7,
60590 Frankfurt am Main, Germany
e-mail: babak.bazrafshan@kgu.de

V. Vogel · W. Mäntele
Institute for Biophysics, Department of Physics,
J.W. Goethe-University, Max-von-Laue-Str 1,
60438 Frankfurt am Main, Germany

Introduction

Tumor thermotherapy methods, among them laser-induced thermotherapy (LITT) [1–7], radio frequency (RF) [2, 8–10], microwave (MW) [10–12], and high-intensity focused ultrasound (HIFU) [13, 14] ablation, are nowadays widely in clinical use. In these methods, tumor cells are heated up to ~80 °C or even higher. At a temperature of ~50 °C, the tissue begins to coagulate, and at higher temperatures, tissue necrosis happens. However, the coagulation process depends not only on the temperature but also on the time; it can take seconds to minutes. These changes in the tumor tissue ensure the death of malicious cells [15–19]. The LITT method is capable of destroying abdominal tumors, e.g., liver metastases, with an improved survival rate and low complication rate of <2 % [20–22]. It is based on the direct transmission of laser energy to the tumor tissue. Based on noninvasive imaging techniques, among them magnetic resonance imaging (MRI), computer tomography (CT), and ultrasound imaging, real-time monitoring and control of the therapy is possible. This enables a more efficient destruction of tumor cells and a better protection of healthy surrounding cells [3, 6, 8–10, 17]. To this end, the imaging-based thermometry can be used as a useful tool.

MRI lacks ionizing radiation and enables a multidirectional scan with a high contrast and resolution; it thus allows for a noninvasive real-time temperature mapping. Different temperature-sensitive MR parameters, including proton resonance frequency (PRF) of the water molecule, T_1 relaxation time, and diffusion coefficient (D), can be used for temperature measurement [15].

The PRF method is based on the fact that the resonance frequency of the hydrogen nucleus (i.e., the proton) in a water molecule depends on the magnetic field in which it is located. In a MRI static magnetic field (B_0), the hydrogen proton experiences a magnetic field which deviates from B_0 due to the electronic screening of the proton. Since the temperature change alters the fraction of the hydrogen bonds to neighboring molecules, the screening of the proton varies. Consequently, the PRF is changed by the temperature [15]. This change is almost linear over a temperature range of −15 to 100 °C [15] and makes the PRF useful for temperature measurement. Other advantages of this method include high temperature sensitivity, temperature accuracy, fast acquisition, and independence on the tissue type except for the fat tissue [23–25]. However, there are some drawbacks to this method such as high sensitivity to motion artifacts [25, 26] and inappropriateness for lipid tissues [27].

The T_1 relaxation time can also be used for temperature estimation. In biological tissues, the water molecule dipolar interaction with surrounding macromolecules causes the spin–lattice relaxation [15]. The corresponding relaxation time, T_1, is a function of the temperature; it increases with temperature rise. This change is linear within a certain temperature range (30–70 °C) [28]. Since this method is more sensitive at low-field strengths, it is favored at low-field scanners [29]. Other advantages of this method include low motion sensitivity and ease of implementation [25]. Nevertheless, since the temperature-induced T_1 change depends on the tissue type (e.g., 1–2 % $°C^{-1}$ for the liver), the thermal coefficient should be determined for each tissue [15, 25].

Thermometry with the diffusion coefficient, D, is based on the thermal random Brownian motion of water molecules which causes the change of D; it increases exponentially with temperature and induces signal attenuation [15]. This method is highly sensitive to temperature (~2 to 2.5 % $°C^{-1}$) and is not affected by the field strength but has a long acquisition time and is highly sensitive to motion [15, 29, 30].

Much effort has been spent over the last years to develop or improve thermometry tools. Previous experiments were conducted in vivo or in vitro employing the LITT, RFA, or HIFU under guidance of MRI or CT [17, 25, 26, 29, 31–37]. However, a comparison of different MR thermometry methods and their compatibility with the LITT ablation has not been performed before in a liver-equivalent phantom. Therefore, in the present study, first, we developed a liver-mimicking polyacrylamide gel phantom as an improved version of the phantom reported in our previous paper [38]. Then, the PRF and T_1 thermometry methods were investigated applying the MR-guided LITT to the gel phantom.

Materials and methods

Phantom preparation

In a previous study of the authors [38], the absorption and MR relaxation properties of the ex vivo porcine liver tissue were identified at different temperatures utilizing spectroscopy and MRI techniques. The absorption spectrum was measured in the range of 750–2,500 nm through the near-infrared spectrometer Spectrum™ 100 N FT-NIR (PerkinElmer, Waltham, MA, USA), and the relaxation times, T_1 and T_2, were determined using the 1.5-T MR scanner Magnetom Espree (Siemens Medical Solutions, Erlangen, Germany). These data were considered as reference to develop a hemoglobin-containing gel phantom for use in thermal ablation experiments.

Here, using the same reference data, methods, and equipment, a MR-compatible liver-equivalent gel phantom was developed. This phantom includes bovine serum albumin (BSA) instead of hemoglobin as absorber of laser photons. Table 1 shows the composition of the phantom as follows: distilled water; the gelling agent Rotiphorese® Gel 40 (29:1)[1] (Roth, Karlsruhe, Germany); the BSA Albumin Fraction V (Roth, Karlsruhe, Germany), which was delivered as a coarse powder and had to be dissolved in the base solution of the phantom, stirring it thoroughly by means of a magnet mixer; the polyvinyl acetate (PVA) microsphere solution Mowilith 0530 S[2] (Celanese, Perstorp, Sweden), which was first diluted in distilled water to a concentration of 30 wt% in order to reduce its viscosity; the MR contrast agents Magnevist®[3] (Bayer HealthCare, Leverkusen, Germany) and Lumirem® (Guerbet GmbH, Sulzbach, Germany) for modification of T_1 and T_2; the two catalysts tetramethylethylenediamine (TEMED) and ammonium persulfate[4] (APS) for activating the polymerization process; NaCl for simulating the electrical conductivity of biological tissues; and sodium azide (NaN_3) for preventing the growth of microorganisms. The phantom solution was mixed very gently in order to prevent the formation of foam and bubbles. Immediately after adding APS, the solution was molded into cone-shaped plastic containers (6.5/4.8–6.2 cm in height/diameter) forming the phantom (5/4.8–5.8 cm in height/diameter) after ~15 min (Fig. 1a).

[1] 40 vol% acrylamide/bisacrylamide; mixture ratio 29:1
[2] 59 wt%; microsphere diameter, 0.45–3.51 μm
[3] 0.5 mmol gadopentetate dimeglumine (Gd-DTPA) in 1 ml Magnevist solution
[4] 10 wt% solution; diluted in distilled water

Table 1 Ingredients of the gel phantom

Substance	Dosage
Distilled water	37.9 vol%
Rotiphorese® (gelling agent)	30 vol%
BSA	16 wt%
PVA microsphere (30 wt% suspension)	10 vol%
Magnevist® (T_1 modifier)	0.04 vol%
Lumirem® (T_2 modifier)	3.3 vol%
TEMED	0.08 vol%
APS (10 wt% solution)	1.75 vol%
NaCl	0.9 wt%
NaN_3	0.03 wt%

Data acquisition and processing

MR imaging for the adjustment of the phantom relaxation times, T_1 and T_2, was conducted with the sequences inversion recovery turbo flash (IRTF) [matrix, 88 × 128 pixels; field of view (FOV), 127 × 185 mm; slice thickness (ST), 5.5 mm; repetition time/echo time/inversion time (TR/TE/TI), 3,000/1.27/100–2,500 ms; flip angle (FA), 15°] and multi-contrast spin echo (matrix, 88 × 128 pixels; FOV, 192 × 280 mm; ST, 5.5 mm; TR/TE, 2,000/10.6–339.2 ms; FA, 180°), respectively. The images were then processed with the software Matlab® R2009b (The MathWorks™, Natick, MA, USA). Two circular regions of interest (ROIs) were selected on each image, inside (34/22 pixels regarding T_1/T_2 images) and outside (138/90 pixels regarding T_1/T_2 images) the phantom (Fig. 1b). Signal intensities (SI) of the T_1/T_2 images, i.e., averaged pixel values in the ROIs, were collected and plotted against TI/TE showing an exponential tendency described as follows:

$$S\ (\mathrm{TI}) = S_0 \cdot \left(1 - 2 \cdot e^{\frac{-\mathrm{TI}}{T_1}} + e^{\frac{-T_{\mathrm{sat}}}{T_1}}\right) \quad (1)$$

and

$$S\ (\mathrm{TE}) = S_0 \cdot e^{\frac{-\mathrm{TE}}{T_2}} + S_1, \quad (2)$$

where S_0 is the intensity at the time origin (TI/TE = 0), T_{sat} in Eq. (1) is the time of the signal saturation, S_1 in Eq. (2) is the intensity at large TE values, and S is the noiseless signal intensity [38, 39]. The latter can be derived from the following:

$$S = \sqrt{\mathrm{SI_{in}}^2 - \mathrm{SI_{out}^2}}. \quad (3)$$

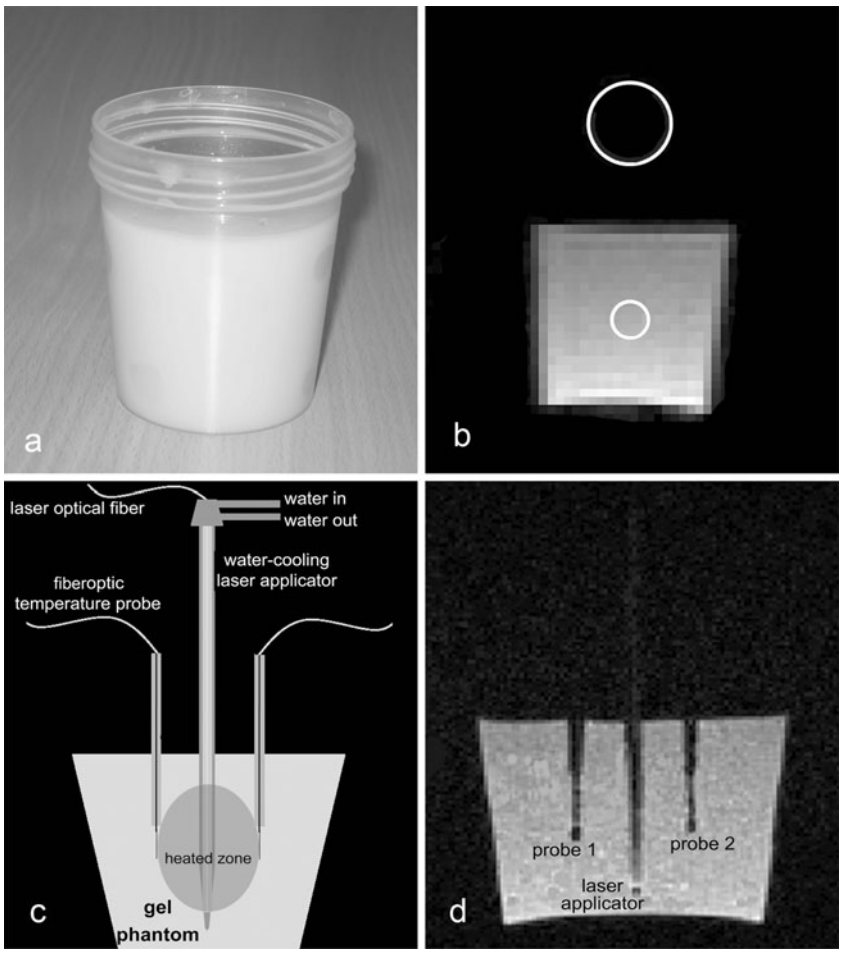

Fig. 1 Gel phantom and experiment setup. **a** The gel molded in plastic container, **b** a MR image showing a cross-section of the phantom as well as the ROIs for recording the phantom signal (*inside*) and the noise (*outside*), **c** experiment setup showing the laser applicator and the two fiber-optic temperature probes inserted in the phantom and the elliptical heated zone around the applicator, **d** a high-resolution MR acquisition for exactly registering the temperature probe tips

Here, the signal intensity in the ROI outside the phantom (SI_{out}) represents background noise and can be subtracted from the phantom signal (SI_{in}) [38, 39]. T_1 and T_2 were determined from the curves described by Eqs. (1) and (2), respectively.

Finally, the phantom was validated comparing it with the liver tissue regarding the temperature dependence of the absorption at λ = 1,064 nm (within 25–95 °C) and relaxation times (within 25–75 °C). As described in the study [38], several samples were fabricated and then heated up in a water bath, each up to a certain temperature in the range of 25–95 °C. The parameters, i.e., absorption and relaxation times, were then measured for/at each sample/temperature. Strength of the linear relationship between the liver and phantom data was examined through the Pearson's correlation test. The data plotting and fitting were performed by the software Origin® (OriginLab, Northampton, MA, USA).

MR-guided LITT in phantom

Experiment preparation and execution

As shown in Fig. 1c, the MR-compatible water-cooled laser applicator Power-Laser-Set 602120 (Somatex® Medical Technologies, Teltow, Germany) was inserted ~4.5 cm into the middle of the phantom sample. An optical fiber (model 602203; Somatex® Medical Technologies, Teltow, Germany) having a diffuser portion of 3 cm was inserted into the applicator in order to deliver the laser photons (λ = 1,064 nm) from a neodymium-doped yttrium aluminum garnet (Nd:YAG) laser device (model MY30; Martin Medizintechnik, Tuttlingen, Germany), operating with a power of 30 W, to the phantom. The mentioned fundamental wavelength of 1,064 nm is typically used in laser ablations due to a higher penetration depth [4, 16, 31, 40]. In order to protect the optical fiber and applicator against high temperatures, the applicator was connected to a water circulating system. A water pump (model GF1200E; Dornier Medizintechnik, Wessling, Germany) was used to circulate the saline solution (0.9 % NaCl) at a flow of 58 ml min^{-1} through a plastic pipe into the applicator. Two fiber-optic temperature probes of the Luxtron 790 thermometer (Luxtron Corporation, Santa Clara, CA, USA) were also inserted into the phantom on both sides of the applicator at a distance of 1.2 ± 0.1 cm from the applicator periphery for temperature measurement during the heating. To insert the probes parallel to the applicator, first, two rigid plastic tubules were inserted into the phantom. The probes were then inserted through the tubules such that they aligned parallel to the applicator, and their tips were ~1 cm outside the tubules and had a direct contact with the gel material. Thereby, it was considered that the probe tips reach the same depth as the middle of the applicator diffuser (i.e., ~3 cm) since the highest temperature is obtained at this point, due to the elliptical shape of the diffuser emission. The Luxtron thermometer uses the Fluoroptic™ effect; a temperature-sensitive phosphorescent sensor is attached to the tip of the probe and detects temperature changes. Temperature accuracy of the device is 0.1 °C, as specified by the manufacturer.

The heating process was monitored at the 1.5-T MR scanner Magnetom Avanto (Siemens Medical Solutions, Erlangen, Germany), utilizing gradient echo sequences including a segmented echo planar imaging (seg-EPI) sequence for the PRF [41] and the following sequences for the T_1 method: fast low-angle shot (FLASH), inversion recovery turbo flash (IRTF), saturation recovery turbo flash (SRTF), and true fast imaging (TRUFI). Using these rapid sequences increases the acquisition speed and consequently minimizes the motion problem [25, 26]. The sequences parameters are listed in Table 2. The parameters were set such that a high image quality and signal to noise ratio (SNR) were achieved within a reasonable acquisition time (TA) of <5 s. In ablation therapies in a moving organ, movement effects can be reduced by choosing such short acquisition times. The resolution, ST, and FOV were chosen the same for all sequences resulting in a voxel volume of ~19 mm^3. Three slices were acquired in all experiments. The seg-EPI sequence collected *k*-space lines of all three slices simultaneously. In order to increase the SNR and temperature sensitivity of the EPI sequence, TE was approximately chosen equal to the T_2* relaxation time of the phantom material at 1.5 T, which was experimentally determined to be 13 ms, and FA was approximately set to the Ernst angle of 50°, given by the Ernst relation as follows [25, 41, 42]:

$$\cos(\mathrm{FA}) = e^{-\frac{\mathrm{TR}}{T_1}}. \quad (4)$$

Thereby, a TR of 155 ms (Table 2) and a T_1 of 300 ms (equal to that of the phantom material at 1.5 T and at room temperature) were considered. Temperature and image acquisition were performed every 5 s until both probes measured a temperature of 70 °C. The process took ~4–5 min each time. The experiment was performed two times with each sequence providing four temperature data sets, since two temperature probes were used in each experiment.

Determination of MR thermal coefficients

Using the Matlab software, the median pixel values within two circular ROIs of 3 pixels, positioned on the images immediately under the probe tips, were read out. The exact position of the probe tips was registered on images acquired through a high-resolution sequence (Fig. 1d) prior to the experiment. Similarly, the values in a further ROI of 18 pixels, selected in an empty region outside the phantom, were read out for noise quantification regarding the T_1 method sequences. For the PRF method, the phase images and, for the T_1 method, the magnitude images were processed. For each sequence, four ROI value data sets were obtained. In case of the T_1 method sequences, the noise was

Table 2 Parameter settings for the MR sequences

	EPI	FLASH	IRTF	SRTF	TRUFI
TR (ms)	155	13	820	820	6.7
TE (ms)	13.3	4.8	1.6	1.6	3.4
TI (ms)	–	–	520	520	–
FA (°)	50	70	20	20	70
FOV (mm)	280 × 280	280 × 280	280 × 280	280 × 280	280 × 280
ST (mm)	4	4	4	4	4
Matrix (pixel)	128 × 128	128 × 128	128 × 128	128 × 128	128 × 128
Bandwidth (Hz/pixel)	399	200	399	399	200
Multi-slice mode	Single shot	–	–	–	–
EPI factor	7	–	–	–	–
Segments	21	–	–	–	–
TA (s)	4.4	4.9	2.9	2.9	2.6

subtracted from the ROI values as described in the last section [Eq. (3)]. In general, to estimate the temperature with the PRF method, the phase shift between a current and a reference phase image is determined. The current temperature can be then calculated by the following [15, 24, 25, 35]:

$$T_{\mathrm{cur}} = \frac{\Delta\phi}{\alpha \cdot \gamma \cdot B_0 \cdot \mathrm{TE}} + T_{\mathrm{ref}}. \quad (5)$$

Here, T_{cur} is the current temperature, T_{ref} is the reference temperature measured at the beginning of heating, α is the PRF shift coefficient (thermal coefficient) in part per million per degree Celsius, $\Delta\varphi$ is the phase shift between a current and the reference image in rad, γ is the gyromagnetic ratio of the water proton (267.5 rad MHz T^{-1}), B_0 is the static magnetic field of the MR scanner (1.5 T), and TE is the echo time, set to the T_2* relaxation time of the phantom material at 1.5 T (13 ms). To determine the thermal coefficient α, three data sets of the ROI values were converted to phase angles, comparing the range of the pixel values on images of [−2,048, 2,048] with the phase angle range of [−π, π] rad. Then, the phase angle was plotted versus temperature up to 70 °C. The term $\Delta\varphi/(T_{\mathrm{cur}} - T_{\mathrm{ref}})$ in Eq. (5) was substituted by the slope of the linear regression of the data points, and α could be then obtained. In case of the T_1 method sequences, the noiseless ROI values (three data sets) were plotted versus their associated temperature data. The thermal coefficient was defined by the slope of a linear fit to data points. The three coefficient values obtained for each sequence were averaged.

Validation of MR thermal coefficients

To determine the temperature through the thermal coefficients, the fourth data set, including ROI values and their associated fiber-optic temperatures, was processed. The PRF temperature was calculated through Eq. (5) using phase angles which were determined by converting the ROI values. The thermal coefficient α, as well as other parameters, was placed in the equation, and the temperature was calculated. For the T_1 method sequences, T_{cur} was calculated as follows:

$$T_{\mathrm{cur}} = \frac{1}{\beta}\Delta S + T_{\mathrm{ref}}. \quad (6)$$

Here, β is the thermal coefficient, and ΔS is the ROI value difference between a current and the reference image acquired at the beginning of the experiment. The standard deviation of the averaged ROI values resulted in an uncertainty of the calculated temperature; the temperature errors were thus approximated by the Gaussian error propagation rule, and then, the root mean square error (RMSE) was determined for each sequence as a measure for temperature precision. Temporal profile of the MR-based temperature was compared with the fiber optic-measured temperature profile. The Bland–Altman analysis was performed to evaluate the agreement between the temperature trends. For each image, the signal to noise ratio (SNR) was calculated as the ratio between the ROI value located in a non-heated part inside the phantom and the noise obtained from the ROI located outside the phantom. The SNR values of each image series were then averaged. SNR of the EPI sequence was calculated also from the magnitude images. All data analyses were performed by the software Origin®.

Results

Phantom parameters evaluation

Absorption

Figure 2a compares the apparent absorption coefficient of the constructed gel phantom and the ex vivo porcine liver tissue, which was considered as reference, within the temperature

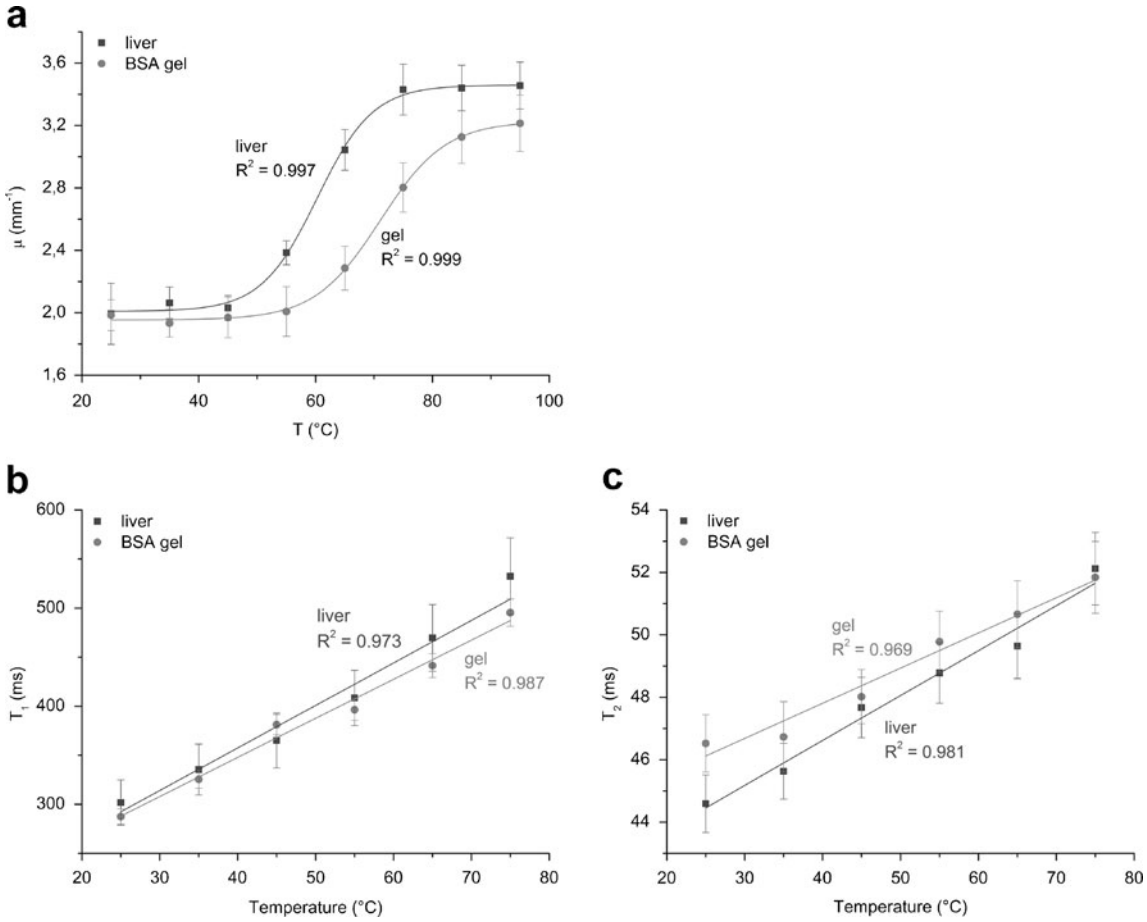

Fig. 2 Comparison between the MR and absorption properties of the phantom material and the liver tissue at different temperatures. **a** Absorption at 1,064 nm, **b** T_1 relaxation time, **c** T_2 relaxation time

range of 25–95 °C. Both fitted curves [R^2 = 0.997/0.999 (liver/gel)] show a sigmoidal behavior with an initial slow change up to ~55 °C followed by a rapid rise to saturation at ~80 °C. However, the absorption of the gel is somewhat lower over the whole temperature range. The error bars indicate the standard deviation (SD) of

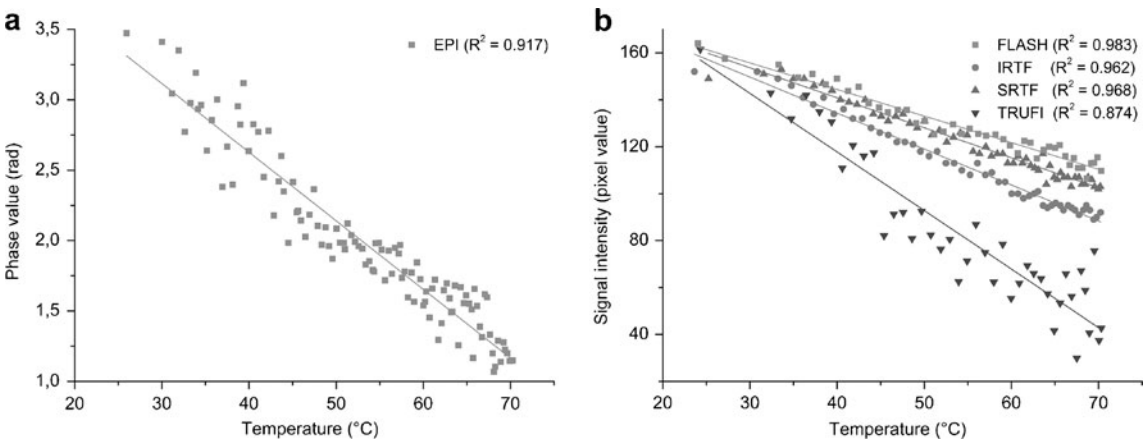

Fig. 3 Phase value (**a**) and signal intensity (**b**) change with temperature of the PRF and T_1 method sequences, respectively. The thermal coefficients were determined from the slopes of the fits to the data points. Demonstrated data correspond to one of the ROI/probe data sets of each sequence. For a better comparison of the slopes, the initial signal values of the T_1 sequences have been normalized to the initial value of the FLASH sequence

averaging the data of three measurements. Pearson's test determined a factor of 0.928 for the correlation between the two data series.

Relaxation times

Comparison between relaxation times of the liver tissue and the gel within the temperature range of 25–75 °C is presented in Fig. 2b (T_1) and Fig. 2c (T_2). The linear fits to the data [with R^2 of 0.973 and 0.987 (T_1) as well as 0.981 and 0.969 (T_2) for the liver and gel, respectively] do not deviate significantly from each other. Nevertheless, a discrepancy is observed for T_1 at higher temperatures and for T_2 at lower temperatures. The Pearson's test revealed a strong positive correlation between the relaxation times of the liver and the gel with coefficients of 0.984 (T_1) and 0.980 (T_2). The error bars are standard deviations of the averaged ROI values.

MR-guided LITT in phantom

Determination of MR thermal coefficients

In Fig. 3, temperature-dependent change of the phase value and signal intensity (with respect to the PRF and T_1 method) of one of the ROI/probe data sets of each sequence are presented. As can be seen, the phase (Fig. 3a) and signal intensity values (Fig. 3b) decay linearly with increasing temperature within the respective temperature range. The thermal coefficients were determined from the slope of the linear fits (Table 3).

Validation of MR thermal coefficients

The temperature calculated through the thermal coefficients is compared with the measured temperature in Figs. 4 and 5 for the EPI, FLASH, IRTF, SRTF, and TRUFI sequences. Figure 4 compares temporal profiles of the two temperatures. In all cases, data points of the MR temperature show almost the same trend as the measured temperature. The RMSE values (Table 4) represent temperature precision of the sequences. The Bland–Altman analysis exhibited in Fig. 5 shows the discrepancy between the two temperatures. Mean of differences (MOD) and limits of agreement (LOA) values are listed in Table 4. MOD values evaluate the systematic main bias and define the temperature accuracy of the sequences. Furthermore, the SNR values of the sequences are also listed in Table 4.

Table 3 Determined thermal coefficients of the MR sequences

	α (ppm °C^{-1})	β (°C^{-1})
EPI	−0.0088 ± 0.0002	–
FLASH	–	−1.15 ± 0.03
IRTF	–	−1.49 ± 0.03
SRTF	–	−1.21 ± 0.03
TRUFI	–	−2.52 ± 0.12

Discussion

To achieve a better control of image-guided tumor ablation therapies, a real-time temperature monitoring is advantageous. For the LITT ablation, due to the compatibility of laser system and applicator with MR scanners, the MR-based thermometry is applicable.

In this study, different MR thermometry sequences were evaluated applying the LITT method to an in-house developed gel phantom which is the modified version of a hemoglobin-based phantom reported by the authors in another paper [38]. The developed phantom here is based on the polyacrylamide and consists of MR contrast agents and BSA for mimicking the properties of the liver tissue, which was confirmed in this paper regarding the absorption coefficient and MR relaxation times. Advantages of this phantom, comparing to those reported in some previous studies [38, 42, 43], are high melting point due to the use of polyacrylamide [38], MR compatibility, and the addition of BSA. The latter is responsible for a liver-like near-infrared absorption in the phantom. In contrast, the mentioned hemoglobin-containing phantom [38] showed a liver-like absorption only at temperatures below 50 °C.

In vitro thermometry experiments in phantom can be helpful to develop and verify real-time temperature-monitoring tools [42]. Advantages of performing the experiments in phantom include simplicity to implement, a homogeneous and well-defined structure as well as reproducibility of the phantom. For these reasons and also due to problems related to the experiments in tissue (e.g., heat-induced structural changes causing possibly large fluctuations of MR image pixel values), it is reasonable to perform thermometry experiments in tissue-mimicking gel phantoms [42].

In order to increase the sensitivity and the SNR of the seg-EPI sequence, TE was set equal to the T_2* relaxation time of the phantom material, and FA was set to the Ernst angle, defined by the Ernst relation [25, 41, 42]. To provide the acquisition consistency, the resolution, slice thickness, and the field of view were set identical for all sequences. The ROIs, whose pixel values were used to determine the thermal coefficients and then temperature, were selected on the images as small as possible and located immediately under the fiber-optic temperature probe tip in order to reduce the effect of temperature gradient within the ROI. Thus, the actual temperature in the ROI did not differ significantly from the measured temperature through the

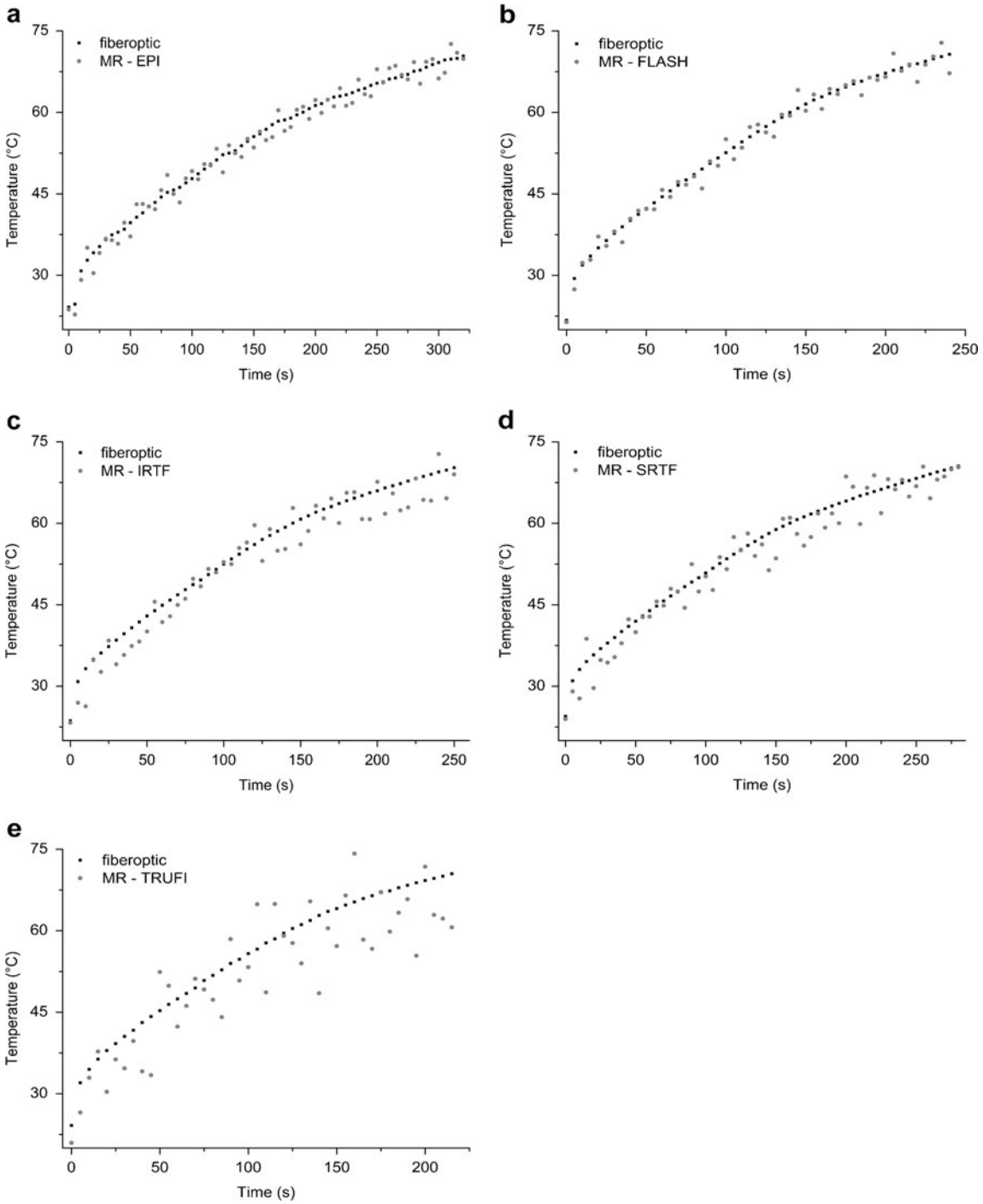

Fig. 4 Comparison of the MR-based and the fiber optic-measured reference temperatures. An agreement is obvious between the temperature trends for the EPI (**a**), FLASH (**b**), IRTF (**c**), SRTF (**d**), and TRUFI (**e**) sequences

probes. To exactly register the probe tips, a high-resolution acquisition was performed prior to each heating experiment.

The observed change of the PRF and the signal intensity with temperature are in accordance with the literature; a linear trend is expected for the PRF method within the range of −15 to 100 °C [15] and for the T_1 method within the range of 30–70 °C [28]. The PRF thermal coefficient of −0.0088 ppm °C^{-1} obtained in this study for polyacrylamide has a difference of 0.0016 with the value reported in some other studies (−0.0072 ppm °C^{-1}) [44, 45]. This discrepancy can be explained by different compositions of the phantoms. Nevertheless, it does not differ significantly from the value of −0.01 ppm °C^{-1} used for water and tissue [15].

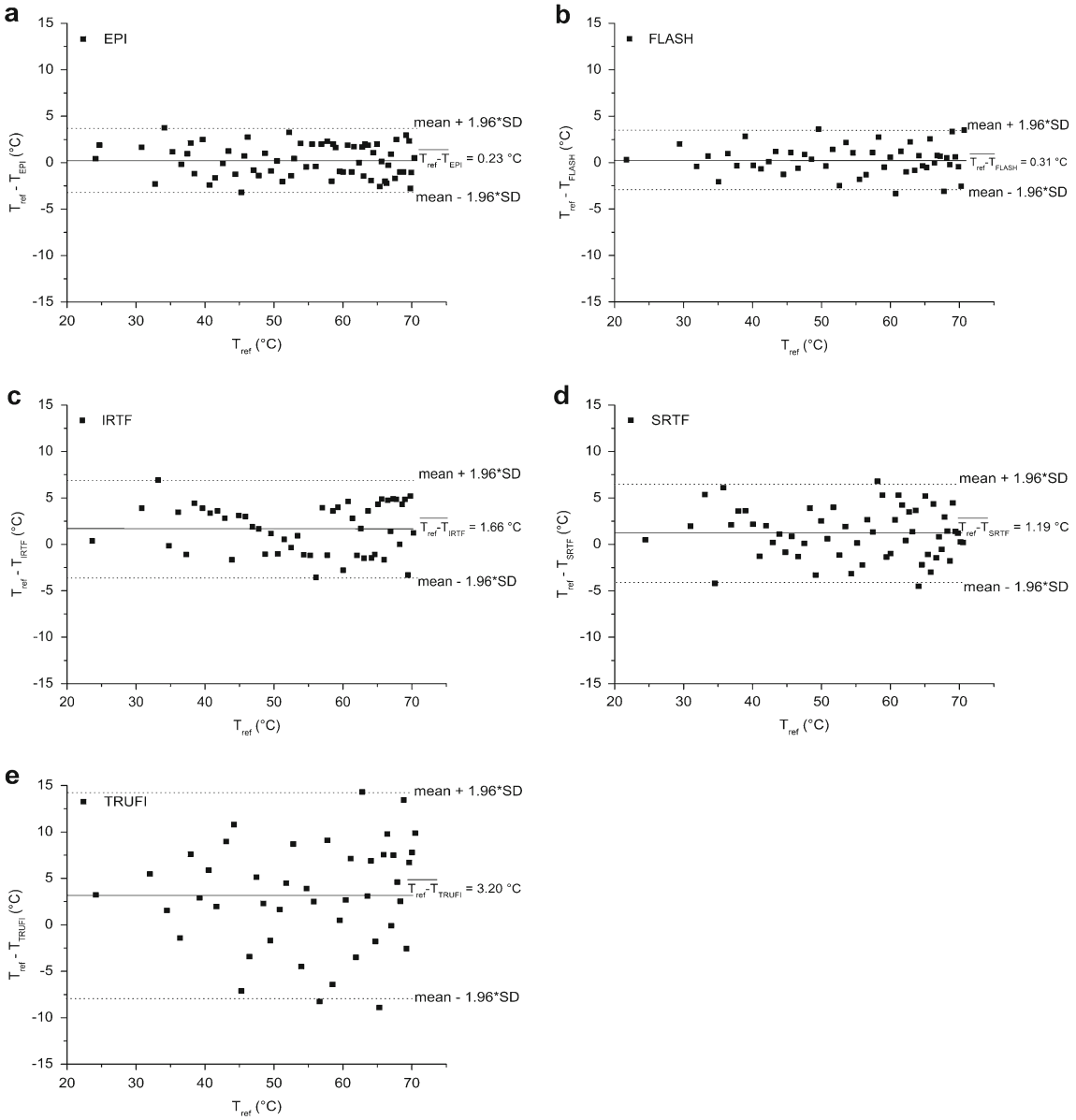

Fig. 5 Difference between the MR-based and the fiber optic-measured reference temperatures is illustrated by the Bland–Altman plots for the EPI (**a**), FLASH (**b**), IRTF (**c**), SRTF (**d**), and TRUFI (**e**) sequences. T_{ref} is the reference temperature measured by the fiber-optic thermometer

Table 4 Comparison between the fiber optic-measured and MR-based temperatures

	Temperature precision (°C)	Bland–Altman		SNR
	(RMSE)	MOD (°C)	LOA (°C)	
EPI	0.60	0.23	3.69/−3.22	67 ± 3
FLASH	0.81	0.31	3.53/−2.91	72 ± 8
IRTF	1.85	1.66	6.89/−3.57	57 ± 11
SRTF	1.95	1.19	6.49/−4.11	54 ± 8
TRUFI	3.36	3.20	14.25/−7.85	28 ± 3

The temperature trends estimated with the thermal coefficients and the fiber optic-measured temperature trends are almost in agreement. According to the RMSE values, EPI and FLASH are the most precise sequences, followed by IRTF, SRTF, and TRUFI. With regards to the temperature sensitivity of the T_1 method sequences, TRUFI is the most sensitive sequence, while FLASH shows the lowest sensitivity, comparing their thermal coefficients. In terms of the accuracy, defined by MOD, EPI and FLASH are again the preferred sequences followed by SRTF, IRTF, and TRUFI. The SNR value of FLASH was measured to be higher than those of other sequences. These results agree, to some extent, with the results reported by Vogl et al. [37]. However, in that paper, IRTF was introduced as the most sensitive and accurate T_1 method sequence (in phantom and at 1.5 T), while in the present study, FLASH was found to be the most accurate sequence for the T_1 thermometry. It should be considered that the agarose phantom prepared in the mentioned study was not examined whether it is liver equivalent, concerning the absorption and MR properties. Furthermore, thermal coefficients were determined during the cooldown period of the phantom which had been preheated up to 60 °C. Some MR parameters including TR, TE, TI, and FA were also chosen differently.

According to the results of the present study, the PRF thermometry method with the seg-EPI sequence is more appropriate for temperature monitoring in the LITT ablation method. This is in accordance to another (not yet published) study that we performed in ex vivo porcine liver tissue. Although it was not examined here, the T_1 method may be more suitable in the case of a homogeneous moving organ such as the liver, by taking the advantage of its relative robustness to motion [25]. To this end, FLASH would be the sequence of choice due to its higher precision and accuracy compared to other T_1 method sequences.

In this preliminary study, we compared the potential of different MR sequences for temperature monitoring during the LITT ablation method using a liver-equivalent phantom. The results are being used to develop a temperature distribution simulation tool and verify its numerical calculations. Developing this tool is a step toward enhancing the noninvasive real-time control of the LITT ablation therapies.

Conclusion

In this study, the PRF and T_1 thermometry methods were investigated performing MR-guided LITT experiments in a liver-mimicking gel phantom. The seg-EPI sequence appeared to be more convenient for temperature estimation, providing a higher precision and accuracy. Among the T_1 method sequences, FLASH was found to be more accurate and robust for temperature imaging of LITT.

Acknowledgments This research was supported by a grant from the Deutsche Forschungsgemeinschaft (DFG) for the project "In-vitro Temperaturbestimmung und Computersimulation der Temperaturverteilung zur optimalen Planung und Steuerung der laserinduzierten Thermotherapie (LITT)," with the reference numbers VO 479/10-2 and SI 1289/1-2, to the institutes IDIR of the J.W. Goethe-University of Frankfurt and the Fraunhofer ITWM.

References

1. Vogl TJ, Mack M, Eichler K, Lehnert T, Nabil M (2009) Effect of laser-induced thermotherapy on liver metastases. Expert Rev Anticancer Ther 6(5):769–774
2. Ferrari FS, Megliola A, Scorzelli A et al (2007) Treatment of small HCC through radiofrequency ablation and laser ablation. Comparison of techniques and long-term results. Radiol Med 112(3):377–393
3. Vogl TJ, Lehnert T, Eichler K, Proschek D, Flöter J, Mack MG (2007) Adrenal metastases: CT-guided and MR-thermometry-controlled laser-induced interstitial thermotherapy. Eur Radiol 17(8):2020–2027
4. Ritz JP, Lehmann KS, Zurbuchen U et al (2007) Improving laser-induced thermotherapy of liver metastases—effects of arterial microembolization and complete blood flow occlusion. Eur J Surg Oncol 33(5):608–615
5. Mensel B, Weigel C, Heidecke CD, Stier A, Hosten N (2005) Laser-induced thermotherapy (LITT) of tumors of the liver in central location: results and complications. Rofo 177(9):1267–1275
6. Vogl TJ, Straub R, Zangos S, Mack MG, Eichler K (2004) MR-guided laser-induced thermotherapy (LITT) of liver tumours: experimental and clinical data. Int J Hyperthermia 20(7):713–724
7. Vogl TJ, Mack MG, Roggan A et al (1998) Internally cooled power laser for MR-guided interstitial laser-induced thermotherapy of liver lesions: initial clinical results. Radiology 209(2):381–385
8. Clasen S, Pereira PL (2008) Magnetic resonance guidance for radiofrequency ablation of liver tumors. J Magn Reson Imaging 27(2):421–433
9. Veltri A, Fazio GD, Malfitana V et al (2004) Percutaneous US-guided RF thermal ablation for malignant renal tumors: preliminary results in 13 patients. Eur Radiol 14:2303–2310
10. Xu HX, Xie XY, Lu MD et al (2004) Ultrasound-guided percutaneous thermal ablation of hepatocellular carcinoma using microwave and radiofrequency ablation. Clin Radiol 59(1):53–61
11. Martin RC, Scoggins CR, McMasters KM (2010) Safety and efficacy of microwave ablation of hepatic tumors: a prospective review of a 5-year experience. Ann Surg Oncol 17(1):171–178
12. Wolf FJ, Grand DJ, Machan JT, Dipetrillo TA, Mayo-Smith WW, Dupuy DE (2008) Microwave ablation of lung malignancies: effectiveness, CT findings, and safety in 50 patients. Radiology 247(3):871–879
13. Pauly KB, Diederich CJ, Rieke V et al (2006) Magnetic resonance-guided high-intensity ultrasound ablation of the prostate. Top Magn Reson Imaging 17(3):195–207
14. Köhrmann KU, Michel MS, Gaa J, Marlinghaus E, Alken P (2002) High intensity focused ultrasound as noninvasive therapy for multilocal renal cell carcinoma: case study and review of the literature. J Urol 167(6):2397–2403
15. Rieke V, Pauly KB (2008) MR thermometry. J Magn Reson Imaging 27(2):376–390
16. Klingenberg M, Bohris C, Niemz MH, Bille JF, Kurek R, Wallwiener D (2000) Multifibre application in laser-induced interstitial thermometry under on-line MR control. Lasers Med Sci 15:6–14

17. Peters RD, Hinks RS, Henkelman RM (1998) Ex vivo tissue-type independence in proton-resonance frequency shift MR thermometry. Magn Reson Med 40:454–459
18. Peller M, Muacevic A, Reinl H et al (2004) MRT-gestützte Thermometrie in der regionalen Tiefenhyperthermie und interstitiellen Laserthermotherapie. Radiologe 44:310–319
19. Thomson S (1991) Pathologic analysis of photothermal and photomechanical effects of laser–tissue interactions. Photochem Photobiol 53(6):825–835
20. Vogl TJ, Eichler K, Straub R et al (2001) Laser-induced thermotherapy of malignant liver tumors: general principals, equipment(s), procedure(s)—side effects, complications and results. Eur J Ultrasound 13(2):117–127
21. Vogl TJ, Straub R, Eichler K, Woitaschek D, Mack MG (2002) Malignant liver tumors treated with MR imaging-guided laser-induced thermotherapy: experience with complications in 899 patients (2520 lesions). Radiology 225:367–377
22. Arienti V, Pretolani S, Pacella CM et al (2008) Complications of laser ablation for hepatocellular carcinoma: a multicenter study. Radiology 246(3):947–955
23. Puccini S, Bär NK, Bublat M, Kahn T, Busse H (2003) Simulations of thermal tissue coagulation and their value for the planning and monitoring of laser-induced interstitial thermotherapy (LITT). Magn Reson Med 49:351–362
24. de Senneville BD, Mougenot C, Quesson B, Dragonu I, Grenier N, Moonen CT (2007) MR thermometry for monitoring tumor ablation. Eur Radiol 17(9):2401–2410
25. Weidensteiner C, Quesson B, Caire-Gana B et al (2003) Real-time MR temperature mapping of rabbit liver in vivo during thermal ablation. Magn Reson Med 50(2):322–330
26. Roujol S, Ries M, Quesson B, Moonen C, de Senneville BD (2010) Real-time MR-thermometry and dosimetry for interventional guidance on abdominal organs. Magn Reson Med 63(4):1080–1087
27. Detti V, Grenier D, Perrin E, Beuf O (2011) Assessment of radiofrequency self-heating around a metallic wire with MR T1-based thermometry. Magn Reson Med 66(2):448–455
28. Hey S, de Smet M, Stehning C et al (2012) Simultaneous T1 measurements and proton resonance frequency shift based thermometry using variable flip angles. Magn Reson Med 67(2):457–463
29. Germain D, Vahala E, Ehnholm GJ et al (2002) MR temperature measurement in liver tissue at 0.23 T with a steady-state free precession sequence. Magn Reson Med 47(5):940–947
30. Lenz C, Klarhöfer M, Scheffler K, Winter L, Sommer G (2011) Assessing extracranial tumors using diffusion-weighted whole-body MRI. Z Med Phys 21(2):79–90
31. Pandeya GD, Klaessens JHGM, Greuter MJW et al (2011) Feasibility of computed tomography based thermometry during interstitial laser heating in bovine liver. Eur Radiol 21:1733–1738
32. de Senneville BD, Roujol S, Moonen C, Ries M (2010) Motion correction in MR thermometry of abdominal organs: a comparison of the referenceless vs. the multibaseline approach. Magn Reson Med 64(5):1373–1381
33. Delabrousse E, Salomir R, Birer A et al (2010) Automatic temperature control for MR-guided interstitial ultrasound ablation in liver using a percutaneous applicator: ex vivo and in vivo initial studies. Magn Reson Med 63(3):667–679
34. Seror O, Lepetit-Coiffé M, Le Bail B et al (2008) Real time monitoring of radiofrequency ablation based on MR thermometry and thermal dose in the pig liver in vivo. Eur Radiol 18(2):408–416
35. Rieke V, Vigen KK, Sommer G, Daniel BL, Pauly JM, Butts K (2004) Referenceless PRF shift thermometry. Magn Reson Med 51(6):1223–1231
36. Peters RD, Chan E, Trachtenberg J et al (2000) Magnetic resonance thermometry for predicting thermal damage: an application of interstitial laser coagulation in an in vivo canine prostate model. Magn Reson Med 44(6):873–883
37. Vogl TJ, Huebner F, Naguib NN et al (2012) MR-based thermometry of laser induced thermotherapy: temperature accuracy and temporal resolution in vitro at 0.2 and 1.5 T magnetic field strengths. Lasers Surg Med 44(3):257–265
38. Bazrafshan B, Hübner F, Farshid P et al (2011) A liver-mimicking MRI phantom for thermal ablation experiments. Med Phys 38(5):2674–2684
39. de Bazelaire CM, Duhamel GD, Rofsky NM, Alsop DC (2004) MR imaging relaxation times of abdominal and pelvic tissues measured in vivo at 3.0 T: preliminary results. Radiology 230(3):652–659
40. Ritz JP, Roggan A, Isbert C, Müller G, Buhr HJ, Germer CT (2001) Optical properties of native and coagulated porcine liver tissue between 400 and 2400 nm. Lasers Surg Med 29(3):205–212
41. Kickhefel A, Roland J, Weiss C, Schick F (2010) Accuracy of real-time MR temperature mapping in the brain: a comparison of fast sequences. Phys Med 26(4):192–201
42. Olsrud J, Wirestam R, Brockstedt S et al (1998) MRI thermometry in phantoms by use of the proton resonance frequency shift method: application to interstitial laser thermotherapy. Phys Med Biol 43(9):2597–2613
43. McDonald M, Lochhead S, Chopra R, Bronskill MJ (2004) Multimodality tissue-mimicking phantom for thermal therapy. Phys Med Biol 49(13):2767–2778
44. d'Arcy JA, Collins DJ, Murphy PS, Rowland IJ, Leach MO (1999) MR thermography using radial sampling. Magn Reson Mater Phy 8(Supplement 1):154
45. Chung YC, Duerk JL, Shankaranarayanan A, Hampke M, Merkle EM, Lewin JS (1999) Temperature measurement using echo-shifted FLASH at low field for interventional MRI. J Magn Reson Imaging 9(1):138–145